Transparency of the atmosphere to short horizontal wavelength gravity waves

Peter Preusse,[1] Stephen D. Eckermann,[2] and Manfred Ern[1]

Received 6 December 2007; revised 27 August 2008; accepted 18 September 2008; published 16 December 2008.

[1] We use theory and global ray modeling to investigate how the potential of gravity waves to transport momentum flux globally from the lower atmosphere into the mesosphere and lower thermosphere (MLT) varies with horizontal wavelength and ground-based phase speed. Ray modeling is performed using the Gravity Wave Regional or Global Ray Tracer (GROGRAT) interfaced to realistic three-dimensional global winds and temperatures from 0 to 100 km altitude, specified by fusing analysis fields at lower altitudes to GCM results higher up. We focus on gravity waves in the short 10- to 50-km horizontal wavelength range that are unresolved by global models and, according to theory, can transport appreciable momentum flux into the MLT. Ray results for different seasons reproduce some of the limits derived from simple wave theory: that horizontal wavelengths shorter than 10 km tend to be removed by vertical reflection or evanescence at the source and slower phase speeds are more prone to critical level removal, leading to a preference for waves with longer horizontal wavelengths and faster ground-based phase speeds to reach the MLT. These findings are compared to the wavelength scales currently resolved by satellite limb and nadir sounders, highlighting wavelength ranges currently measured and those currently unresolved. A road map is developed for how current and future satellite measurements can be combined to measure the full space-time spectrum of gravity waves relevant to eddy flux deposition and momentum forcing of the global MLT. In particular, recommendations for new satellite measurement strategies that fill current measurement gaps are provided.

Citation: Preusse, P., S. D. Eckermann, and M. Ern (2008), Transparency of the atmosphere to short horizontal wavelength gravity waves, *J. Geophys. Res.*, *113*, D24104, doi:10.1029/2007JD009682.

1. Introduction

[2] On parameterizing the effects of breaking gravity waves (GWs) in a global numerical model for the first time, *Holton* [1982] was able to reproduce the wind and thermal structure of the mesosphere and lower thermosphere (MLT). Since then it has become established that GWs are the main dynamical driving force for the MLT [*McLandress*, 1998; *Fritts and Alexander*, 2003]. However, the evidence from modeling studies is indirect and based on matching observed global wind fields (e.g., zonal mean wind climatologies) with output from general circulation models (GCMs).

[3] It is obviously preferable to derive wave-induced global mean-flow driving directly from measurements of actual gravity wave motions in the atmosphere. However, measurement of gravity waves from space has been highly problematic until comparatively recently (see Table 1 and *Wu et al.* [2006] for an overview). Certain satellite remote-sensing techniques resolve only portions of the full space-time gravity wave spectrum, and it remains unclear which wavelength scales from which measurements are most relevant to momentum flux deposition in the MLT. Thus, our goal in this paper is first to estimate, as best we can from modeling, which gravity wave wavelengths are capable of transporting and depositing momentum flux in the MLT, and then to assess the status of current satellite remote sensors in resolving these flux-carrying portions of the gravity wave spectrum. Our purpose is to provide theoretical guidance for the design of next-generation satellite remote-sensing instruments and integrated missions capable of resolving the relevant gravity wave wavelength ranges responsible for driving the MLT. In other words, is it possible with state-of-the-art technology to measure all the relevant scales of GWs from space and, if so, which remote-sensing techniques have to be combined to achieve this aim?

[4] The relevant scales to observe are determined by how GW momentum flux varies as a function of horizontal and vertical wavelength, but owing to the lack of global observations it is unclear which part of the gravity wave spectrum conveys which fraction of the total vertical flux of horizontal momentum into the MLT. In particular, GWs of almost any horizontal wavelength could provide sufficient drag to explain the temperature and wind structure of the MLT, if they occur sufficiently frequently (see below). Therefore we

[1] Institut für Chemie und Dynamik der Geosphäre, ICG-1: Stratosphäre, Forschungszentrum Jülich GmbH, Jülich, Germany.
[2] Space Science Division, Naval Research Laboratory, Washington, D. C., USA.

0148-0227/08/2007JD009682

Table 1. Overview of Satellite Instruments Used for GW Studies

Technique	Instrument	Full Name	Selected References
Infrared limb sounding	LIMS	Limb Infrared Monitoring of the Stratosphere	*Fetzer and Gille* [1994]
	CRISTA	Cryogenic Infrared Spectrometers and Telescopes for the Atmosphere	*Eckermann and Preusse* [1999] *Preusse et al.* [2002] *Ern et al.* [2004]
	CLAES	Cryogenic Limb Array Etalon Spectrometer	*Preusse and Ern* [2005]
	SABER	Sounding of the Atmosphere using Broadband Emission Radiometry	*Preusse et al.* [2006]
	HIRDLS	High Resolution Dynamics Limb Sounder	*Alexander et al.* [2008]
GPS radio occultation	GPS-MET		*Tsuda et al.* [2000]
	CHAMP	CHAllenging Minisatellite Payload	*de la Torre et al.* [2006]
Microwave saturated limb radiances	UARS/MLS	Upper Atmosphere Research Satellite/Microwave Limb Sounder	*Wu and Waters* [1996] *McLandress et al.* [2000] *Jiang et al.* [2004]
	AURA/MLS	EOS-AURA/Microwave Limb Sounder	*Wu and Eckermann* [2008]
Infrared sublimb view	MSX/MWIR	Midcourse Space Experiment/Mid-Wavelength Infrared Radiometer	*Dewan et al.* [1998]
Infrared nadir view	AIRS	Atmospheric Infrared Sounder	*Alexander and Barnet* [2007]
Microwave nadir view	AMSU	Advanced Microwave Sounding Unit	*Wu and Zhang* [2004] *Eckermann et al.* [2006]

should ideally design our instruments to measure all scales of GWs which potentially can propagate from the forcing altitude into the MLT. Fortunately there are physical limits on the range of wavelength scales for freely propagating GWs.

[5] The intrinsic frequency $\hat{\omega}$ of a GW is limited by the relation

$$N > |\hat{\omega}| > |f|, \tag{1}$$

where N is the buoyancy frequency and f is the Coriolis parameter. The frequency limit (1) implies horizontal wavelength limits. The Coriolis parameter inhibits long horizontal wavelength GWs at high and mid latitudes and we therefore observe an increase of the average horizontal wavelength toward low latitudes [*Alexander et al.*, 2002; *Ern et al.*, 2004; *Wang et al.*, 2005]. Experience shows that these long horizontal wavelength GWs in the tropics can be observed from space (e.g., *Ern et al.* [2004] and section 5). More challenging to observe are waves close to the short wavelength limit. If the intrinsic frequency $\hat{\omega}$ approaches the buoyancy frequency N, the wave is reflected or is evanescent at its source (the latter hereafter referred to simply as an evanescent GW). There is a minimum horizontal wavelength for those waves which can propagate upward. In section 2 we review previous work [e.g., *Schoeberl*, 1985; *Iwasaki et al.*, 1989; *Marks and Eckermann*, 1995; *Kim et al.*, 2003] on how a short horizontal wavelength boundary can be estimated from the dispersion relation. This wavelength limit depends on the intrinsic frequency of the GWs and on the buoyancy frequency and therefore varies with altitude, location and season. For intrinsic phase speeds slower than 150 m s^{-1} the horizontal wavelength limit varies between 10 and 50 km given typical stratospheric conditions [*Alexander and Dunkerton*, 1999].

[6] The primary focus of this paper is therefore to investigate the short horizontal wavelength boundary due to wave reflection and wave evanescence and its variations in a realistic three-dimensional atmosphere and for different seasons. In this paper we restrict attention to those GWs that can freely propagate upward. Of course it would be more interesting to investigate how the various limits affect the GW-induced background wind acceleration. However, this requires knowledge of the source distribution and on global scale the shape of the source spectrum and the intermittency of various wave sources is not well known.

[7] In particular, it is impossible to infer from the available evidence whether very short horizontal wavelength waves (horizontal wavelengths λ_h smaller $\sim$100 km) or mesoscale and long horizontal wavelength GWs (horizontal wavelengths λ_h longer $\sim$100 km) dominate the driving of the MLT. For the longer horizontal wavelengths global information has been provided by satellites and GW resolving global models. However, uncertainties are still large. For the short horizontal scales we have evidence in particular from observational case studies and regional modeling. Here the primary source of uncertainty is to extrapolate results from these local events to a global-scale momentum flux budget. In the following paragraphs we give a brief overview of the effects of GWs in global models and of the evidence we have for short and long horizontal wavelength GWs, respectively.

[8] The interaction of a GW with the background flow is governed primarily by its horizontal phase speed and depends only weakly on it's horizontal wavelength [e.g., *Hines*, 1997; *Warner and McIntyre*, 2001; *Fritts and Alexander*, 2003]. For instance, the *Hines* [1997] parameterization integrates over a horizontal wave number spectrum to yield a single ''characteristic'' horizontal wavelength for the GW spectrum. In GCM studies typical values range from $\sim$60 km (shortest values used by *Manzini and McFarlane* [1998] and *Akmaev* [2001]), and 125 km [*Charron et al.*, 2002], to several hundred kilometers (*Manzini et al.* [1997] and longest values used by *Manzini and McFarlane* [1998] and *Akmaev* [2001]). This shows that longer horizontal wavelength GWs could conceivably provide sufficient momentum to drive the MLT. However, since a large number of partly compensating tuning parameters is used in the Hines scheme, these choices do not provide any compelling evidence for preferential GW horizontal wavelengths [*Akmaev*, 2001; *Fritts and Alexander*, 2003].

[9] The Warner and McIntyre GW parameterization scheme [*Warner and McIntyre*, 2001] implicitly integrates over a wide range of intrinsic wave frequencies $\hat{\omega}$, thus including both short and long horizontal wavelength GWs. *Ern et al.* [2005] isolated the longer wavelength portion ($\lambda_h \geq 100$ km) of the assumed semiempirical horizontal wavelength spectrum, which reduced the momentum flux by about a factor of two [see *Ern et al.*, 2005, Figures 2c and 2d], indicating that the two horizontal wavelength ranges might be of equal importance for mean-flow driving.

[10] *Hamilton et al.* [1999] enhanced the spatial resolution of a GCM to a degree that a realistic middle atmosphere was reproduced without employing GW parameterizations. The highest horizontal grid resolution was 30 km. With increasing computer power more models will be run at these kinds of high spatial resolutions. However, spectral analysis of output from these models reveals that the wave momentum flux spectrum is still not fully resolved indicating an ongoing need for GW drag parameterization [see *Kim et al.*, 2003, section 6c]. The realism of the gravity waves spontaneously generated and explicitly resolved in high-resolution global models is unclear [e.g., *Horinouchi et al.*, 2003]. Thus, before high-resolution model results can be interpreted in order to understand GWs in the real atmosphere, they need to be validated by global measurements, as must the GW drag parameterizations used in low-resolution models. In all cases, satellite measurements of GWs are absolutely critical for validation.

[11] Satellite and long-duration balloon estimates of GW momentum flux [*Ern et al.*, 2004, 2006; *Vincent et al.*, 2007; *Alexander et al.*, 2008] reveal GWs carrying considerable momentum flux. However, GW momentum flux estimates from current generation satellites still suffer from relatively coarse spatial sampling [*Ern et al.*, 2004] and accordingly have too large uncertainties in their momentum flux estimates for calculating reliable vertical gradients. Therefore mean flow acceleration was not estimated from these data. Nevertheless, the satellite and long-duration balloon observations clearly indicate that longer horizontal wavelength GWs are important for the total GW momentum flux.

[12] Short horizontal wavelength GWs ($\lambda_h \leq 100$ km) have fast vertical group velocities and therefore can rapidly propagate from the troposphere into the MLT. In addition, the vertical flux of horizontal pseudo momentum density of a GW is proportional to its horizontal wave number (i.e., inversely proportional to λ_h). Thus, where short horizontal wavelength GWs are present in the atmosphere, they can theoretically carry significant wave momentum. Accordingly, *Alexander and Dunkerton* [1999] found that wave reflection can have a large influence on the GW induced acceleration of background winds in the MLT, if a spectrum that favors short horizontal wavelengths is assumed.

[13] A prominent source for short horizontal wavelength GWs is deep convection. High-resolution simulations of convection and squall lines show that isolated deep convective systems force predominantly short horizontal wavelengths [*Fovell et al.*, 1992; *Piani et al.*, 2000; *Lane et al.*, 2001]. Circular wave fronts like the ones predicted by convective models have been observed in satellite sublimb data [*Dewan et al.*, 1998] as well as in MLT airglow imagery [*Taylor et al.*, 1987; *Taylor and Hapgood*, 1988; *Sentman et al.*, 2003; *Suzuki et al.*, 2007a]. However, other models and mechanisms of GW generation by deep convection predict the generation of longer horizontal wavelength GWs [*Salby and Garcia*, 1987; *Pfister et al.*, 1993] and such waves have also been observed in situ [*Pfister et al.*, 1993] and from satellites [*Preusse et al.*, 2001; *Jiang et al.*, 2004; *Preusse and Ern*, 2005].

[14] A second prominent source of GWs is wind flow over orography exciting mountain waves. Mountain waves have been extensively studied over decades (see, e.g., the early work by *Queney* [1948] and reference papers by *Fritts and Alexander* [2003] and *Kim et al.* [2003]). Depending on details of the topography all horizontal scales from a few kilometers to several hundred kilometers can be forced and have been observed in the upper troposphere and stratosphere [e.g., *Nastrom and Fritts*, 1992; *Dörnbrack et al.*, 2002; *Eckermann et al.*, 2007; *Alexander and Barnet*, 2007].

[15] The most convincing evidence for short horizontal wavelength is provided from the combination of air glow images with radar measurements of the background wind. These data have been evaluated for momentum flux in the MLT. Peak flux magnitudes per unit mass can be as high as 400 to 900 $m^2\ s^{-2}$ [*Smith et al.*, 2006; *Fritts et al.*, 2002] and accelerations may reach up to 80 $m\ s^{-1}$ in 1 hour. However, nightly or monthly averages are much smaller. The stations measuring momentum flux report nightly or monthly averages (peak values) of: Starfire Optical Range in New Mexico, 30 $m^2\ s^{-2}$ (10–100 $m^2\ s^{-2}$) [*Swenson et al.*, 1999; *Tang et al.*, 2002]; Shigaraki in Japan, 5 $m^2\ s^{-2}$ (20 $m^2\ s^{-2}$) [*Suzuki et al.*, 2007b]; Hawaii, 2 $m^2\ s^{-2}$ (nightly averages 0–5 $m^2\ s^{-2}$) [*Tang et al.*, 2005]; Halley at Antarctica, 6–10 $m^2\ s^{-2}$ [*Espy et al.*, 2004]; and Rothera at Antarctica, 10–40 $m^2\ s^{-2}$ [*Espy et al.*, 2006]. The local enhancement above the Antarctic Peninsula (Rothera) is also found at lower altitudes for longer horizontal wavelengths in satellite data [e.g., *Fetzer and Gille*, 1994; *Eckermann and Preusse*, 1999; *Jiang et al.*, 2002; *Ern et al.*, 2004], while Hawaii is located at a local minimum of subtropical convectively generated GW activity [e.g., *Jiang et al.*, 2004; *Ern et al.*, 2004]. Assuming these short horizontal wavelength GWs completely deposit their momentum in a 20-km-wide vertical altitude region, at Halley, Rothera and New Mexico they would contribute a significant fraction of the total wave drag. At some places (e.g., Rothera, New Mexico) the observed momentum of the short wavelength GWs alone might suffice to drive the MLT, if these values were representative of the zonal means. However, the examples also show that global observations are required for the interpretation of these few, isolated measurements.

[16] The evidence for short horizontal wavelength GWs stems from local observations and modeling. Estimating global momentum flux from these isolated sources naturally implies large uncertainties. Can global GW-resolving modeling with high resolution GCMs now or in the near future close this gap? *Lane and Knievel* [2005] show that the GW momentum flux over deep convection only converges at a model horizontal grid resolution of 500 m. In addition, the types of GWs forced by convection in global models depends to a large degree on the ways in which deep

convection is parameterized. Different parameterizations can yield enormous differences in the nature of the forced waves, suggesting considerable unreality in explicitly resolved GWs in global models [e.g., *Horinouchi et al.*, 2003]. Thus reliable global modeling from this source is at present infeasible.

[17] The horizontal wavelength distribution of those GWs which drive the MLT, if known, would be highly relevant for GW drag parameterizations. Though GWs of the same phase speed and amplitude but with different horizontal wavelengths break in a broadly similar fashion within similar background wind conditions (the basis of several GW parameterizations, see above), they follow different propagation paths from low to high altitudes and carry and deposit different momentum fluxes.

[18] Answering this question about the most relevant horizontal GW scales requires global observations of the whole spectrum of those GWs with the potential to transport wave momentum from the troposphere or tropopause into the MLT. True global coverage is only provided by satellite instruments and an increasing number of different instruments and techniques are now exploited for GW studies. An overview of GW satellite observations is given by *Wu et al.* [2006]. Table 1 summarizes different techniques, the respective instruments and selected scientific citations.

[19] Could we observe all the upward propagating GWs in the middle atmosphere if we were to combine observations by different remote-sensing techniques? In order to answer this question, we first need to know which GWs are able to propagate upward into the MLT. Gravity waves can have very small spatial scales and some waves lie outside the visibility limit of any current satellite instrument. However, GWs with very small scales cannot propagate far vertically in the atmosphere and therefore have very limited potential for coupling the upper troposphere with the mesosphere.

[20] In this paper we derive theoretical lower limits for the horizontal and vertical wavelengths of those gravity waves which can propagate upward into the MLT. Previous studies have estimated these limits using highly idealized wave equations and climatological background atmospheres [e.g., *Schoeberl*, 1985; *Iwasaki et al.*, 1989; *Kim et al.*, 2003]. Here we perform a more comprehensive and realistic modeling study which traces gravity waves globally from the troposphere to MLT using detailed ray tracing and realistic, three-dimensional specifications of the background global atmosphere from 0 to 100 km altitude for 4 days in 2003, representative of spring, summer, fall and winter conditions. We investigate latitudinal and seasonal variations of the horizontal and vertical wavelength boundaries. We use the limits resulting from this modeling to develop a road map for the optimal combination of instruments on a GW-dedicated satellite mission.

[21] Section 2 summarizes basic GW equations and outlines the physical laws limiting GW propagation. Section 3 describes the model experiments employing the Gravity wave Regional Or Global RAy Tracer (GROGRAT) [*Marks and Eckermann*, 1995; *Eckermann and Marks*, 1997] and section 4 infers from the model results which fraction of waves reaches 80 km and 100 km altitude, respectively, the reasons why rays cease propagating upward, and how this varies with latitude and season. Section 5 discusses the prospects of gaining global information from satellite remote sensors on the different scales of GWs which potentially can convey momentum from the troposphere into the MLT, and section 6 summarizes the results.

2. Basic Theory

[22] Evanescence and reflection of GWs are governed by the GW dispersion relation, which is also the basis of the GROGRAT ray tracer. A fairly general form of the dispersion relation for GWs takes the form [*Marks and Eckermann*, 1995]

$$\hat{\omega}^2 = \frac{N^2 k_h^2 + f^2(m^2 + \alpha^2)}{k_h^2 + m^2 + \alpha^2}, \tag{2}$$

where $k_h = (k^2 + l^2)^{1/2}$ is total horizontal wave number (k and l are the zonal and meridional components, respectively), m is vertical wave number, N is background buoyancy frequency, f is inertial frequency, and $\alpha = \frac{1}{2H_\rho}$, where H_ρ is density scale height. The GW intrinsic frequency is

$$\hat{\omega} = \omega - ku - lv = k_h \hat{c}, \tag{3}$$

where the intrinsic horizontal phase speed is

$$\hat{c} = c - U\cos(\phi). \tag{4}$$

[23] Here $U = (u^2 + v^2)^{1/2}$ is the total horizontal wind speed (u and v are the zonal and meridional components, respectively), ω is ground-based frequency, $c = \omega/k_h$ is the ground-based horizontal phase speed, and ϕ is the angle between the horizontal wind direction and the horizontal wave propagation direction.

[24] In the limit of short horizontal wavelengths and higher intrinsic frequencies, and assuming $N^2 \gg f^2$, then (2) simplifies to

$$\hat{\omega}^2 = \frac{N^2 k_h^2}{k_h^2 + m^2 + \alpha^2} \Leftrightarrow m^2 = \frac{N^2}{\hat{c}^2} - \left(k_h^2 + \alpha^2\right). \tag{5}$$

[25] An upward propagating wave experiences varying winds so that $\hat{c}$ changes according to (4), as well as vertically varying buoyancy frequency N. A gravity wave can be reflected at a turning level where $m^2 \to 0$, which from (5) occurs at a critical horizontal wavelength

$$\lambda_{h,crit} = 2\pi \frac{|\hat{c}|}{\sqrt{N^2 - \alpha^2 \hat{c}^2}}. \tag{6}$$

[26] We see from (6) that the very smallest values of this critical wavelength occur when $N^2 \gg \alpha^2 \hat{c}^2$, so we approximate the absolute short horizontal wavelength limit as

$$\lambda_{h,crit} = 2\pi \frac{|\hat{c}|}{N}. \tag{7}$$

[27] The expression on the right of (7) is simply the hydrostatic expression for the vertical wavelength. For a

typical tropospheric value of $N = 0.01\ s^{-1}$, (7) tells us that the shortest horizontal wavelength is $\sim 0.628\hat{c}$ kilometers, for $\hat{c}$ values in meters per second.

[28] The maximum vertical flux of horizontal pseudo momentum density that can be carried by a GW depends on both the horizontal and vertical wavelength. Following *Ern et al.* [2004] the vertical flux of horizontal pseudo momentum density F_p of a monochromatic GW is proportional to its vertical and inversely proportional to its horizontal wavelength as well as proportional to the square of the temperature amplitude $\hat{T}$,

$$F_p \propto \frac{\lambda_z}{\lambda_h}\hat{T}^2. \tag{8}$$

[29] Since the amplitude saturation limit $\hat{T}_{\max}$ due to static instability is also proportional to the vertical wavelength [*Eckermann and Preusse*, 1999]

$$\hat{T}_{\max} = \frac{\lambda_z}{2\pi}\frac{\overline{T}}{g}N^2, \tag{9}$$

the maximum momentum flux that can be carried by a wave is proportional to the third power of the vertical wavelength [*Preusse et al.*, 2006],

$$F_{p,\max} \propto \frac{\lambda_z^3}{\lambda_h} = \frac{k_h}{m^3}. \tag{10}$$

[30] Thus, (10) tells us that, for waves of a given peak temperature amplitude, the largest momentum fluxes are carried by those waves with short horizontal and long vertical wavelengths. Of course source and saturation processes also affect the distribution of temperature variance among waves of different horizontal and vertical wavelengths [e.g., *Tsuda et al.*, 1991; *Bacmeister et al.*, 1996].

3. Ray Modeling

[31] A full description of the GROGRAT model is given by *Marks and Eckermann* [1995] and *Eckermann and Marks* [1997]. Briefly, the model uses the nonhydrostatic, rotational GW dispersion relation of the form in equation (2). The resulting ray-tracing equations take into account horizontal as well as vertical refraction of the wave vector due to gradients of the background wind and temperature fields. Temporal variations of the atmospheric background can also be explicitly taken into account, but are neglected here since a static background atmosphere is assumed. A wave is traced upward as long as GW physics allows the free propagation of the wave and as long as the ray remains in the domain where a background atmosphere is provided. A detailed discussion of the different physical and technical conditions which cause GROGRAT to terminate a ray trace are discussed below.

[32] Strictly speaking GW ray tracing may be only applied where the WKB approximation is satisfied. Therefore GROGRAT normally uses threshold criteria to terminate rays when the WKB assumption is violated. This does not mean, however, that in the real world the wave cannot further propagate and many ray models trace waves through such limits [e.g., *Schoeberl*, 1985]. The WKB approximation states that the background atmosphere changes slowly compared to the wavelength of the waves. This is more likely violated for fast phase-speed, long vertical wavelength waves. Therefore the standard WKB termination of the rays poses a problem in our study. If we include the WKB-terminated waves in our statistics, we bias our results, because we introduce a termination criterion which would not prevent real waves from further propagating, and if we exclude these waves completely from the statistics, we bias our results, because the WKB criterion will more often be violated for reflected waves. Since in this study wavelength statistics and not the details of the ray path is our primary focus, we decided to disregard the WKB thresholds and continue the wave propagation past WKB limits.

[33] Wave amplitudes along the rays are calculated using conservation of vertical wave action flux densities and are dissipated using scale-dependent radiative damping, background turbulent diffusion, and one of several available wave saturation schemes, which all tend to have largest effects on short vertical wavelength gravity waves near critical levels. To speed up the calculations, waves slowly propagating toward their critical level singularity are identified and removed using a minimum wave amplitude criterion and a minimum vertical group velocity criterion (see Appendix A for the sensitivity of the results to the minimum amplitude criterion). Waves that reflect vertically are identified using the normalized parameter $m^{-2}\frac{\partial m}{\partial z}$ which, when significantly greater than unity, identifies breakdown of the WKB approximation, which clearly occurs as $m^2 \rightarrow 0$. See *Marks and Eckermann* [1995] for further details.

[34] The aim of the modeling study is a global investigation of GW propagation with a particular focus on short horizontal wavelength GWs. The model setup follows that described by *Preusse et al.* [2006], but uses shorter horizontal wavelengths at the source. Rays were launched either at 5 km or 20 km altitude, in eight different horizontal propagation directions, every 5° latitude and every 20° longitude. The rays are launched for each spectral component to be investigated. One spectral component experiment (SCE) is defined by the ground-based phase speed c and the horizontal wavelength λ_h. Six phase speeds of c = 3, 6, 10, 20, 30 and 50 m s^{-1} and horizontal wavelengths of λ_h = 10, 25, and 50 km are launched at both source altitudes. In order to enhance the resolution in horizontal wavelength close to $\lambda_{h,crit}$, additional rays were launched with λ_h = 40 km at the 5 km launch level and with λ_h = 18 km at the 20 km launch level for all phase speeds. We have also performed some sensitivity tests on the choice of launched phase speeds. The results of the sensitivity tests can be found in Appendix B.

[35] The background atmosphere (wind, temperature and geopotential height fields) is specified from ECMWF analysis data for altitudes below 55 km and output from a thermosphere-ionosphere-mesosphere-electrodynamics general circulation model (TIME-GCM) [*Roble and Ridley*, 1994] experiment for altitudes 40–100 km. ECMWF reanalysis data are used in numerous transport studies and capture the synoptic-scale features of the troposphere and stratosphere well [*Borsche et al.*, 2007; *Ern et al.*, 2007]. In order to reproduce the actual atmospheric state, the TIME-GCM run

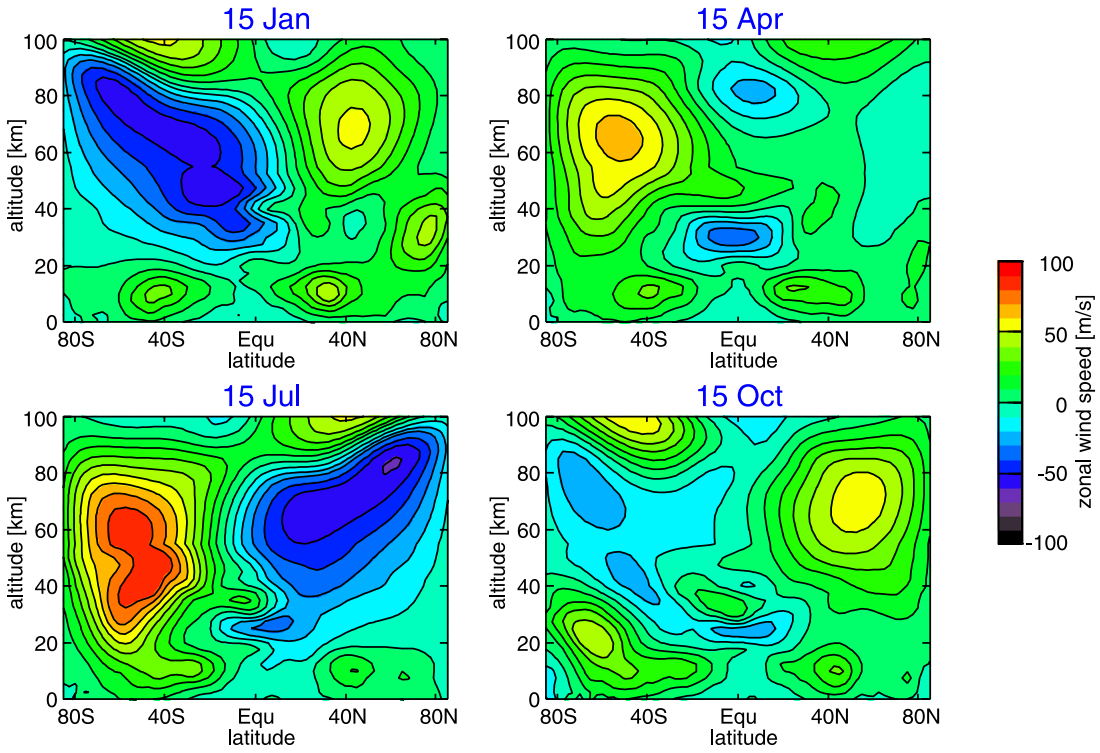

Figure 1. Zonal mean zonal winds for 15 January, 15 April, 15 July, and 15 October 2003. The data are zonal averages of the wind fields used for the ray-tracing experiments and composed from ECMWF data below 55 km and a TIME-GCM experiment above 40 km with a smooth transition at the overlapping altitudes.

was nudged at 30 km altitudes to NCEP reanalyses and radiation-forced migrating tidal components at the lower boundary are provided from the GSWM tidal model [*Hagan et al.*, 1995]. The GCM was run continuously from January 2002 to December 2004 in support of the TIMED mission [*Oberheide et al.*, 2006].

[36] At the overlapping altitudes of 40–55 km a smooth transition from ECMWF to TIME-GCM fields is achieved

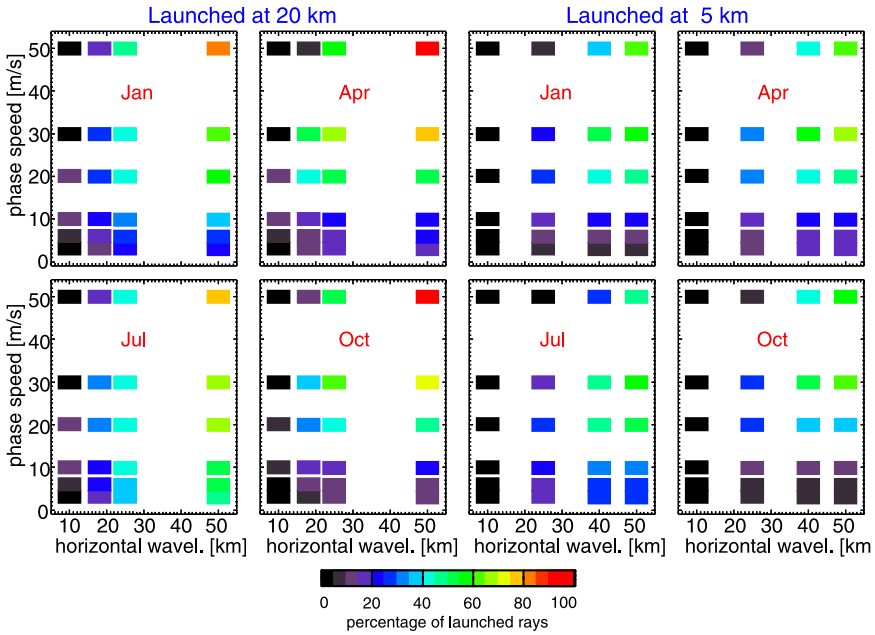

Figure 2. Percentage of rays which reach altitudes of 80 km or higher (left) for 20 km launch altitude and (right) for 5 km launch altitude. Values for (top) 15 January and 15 April 2003 and (bottom) 15 July and 15 October 2003.

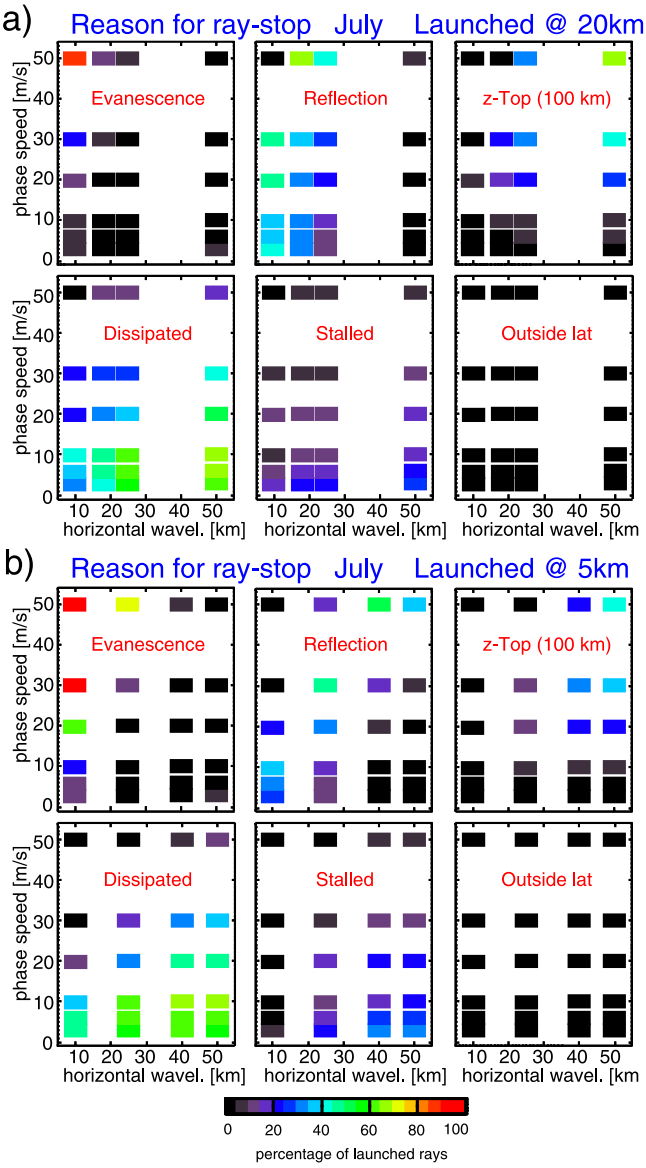

Figure 3. Reason why rays were terminated by GROGRAT: (a) results for rays launched at 20 km altitude and (b) results for rays launched at 5 km altitude; background atmosphere is for 15 July 2003. For details, see text.

by calculating a weighted mean of the two data sets, where the height-varying weight of the ECMWF data is 1 at 40 km altitude and drops linearly to zero at 55 km altitude and vice versa for the TIME-GCM data. Figure 1 shows the resulting zonal mean zonal winds for 15 January, 15 April, 15 July and 15 October 2003. The wind fields reproduce salient climatological features and thus demonstrate that this fused data set realistically represents important atmospheric structures such as the polar jets, the wind reversal above the summer mesosphere and the quasi biennial oscillation (QBO) in the tropical stratosphere.

[37] ECMWF and TIME-GCM data are merged after interpolation onto a common grid of 2.5° latitude, 3.75° longitude and 41 pressure levels corresponding to an approximate pressure altitude spacing of 2.5 km. These atmospheric fields are ingested into GROGRAT and internally reinterpolated onto a regular geometric height grid every 2.5 km from 0.5 km to 100.5 km. Latitude coverage is from 85°S to 85°N.

4. Results

4.1. Spectral Dependencies

[38] Figure 2 shows globally averaged percentages of all the rays which reach at least 80 km altitude and thus have potential to carry GW momentum from low altitudes into the MLT. The x axis gives the horizontal wavelength at launch altitude, the y axis gives the ground-based horizontal phase speed.

[39] From criterion (7) for $N \simeq 0.01$ s^{-1} (0.02 s^{-1}) we would expect that, for a 10 km horizontal wavelength, GWs with intrinsic phase speeds faster than $\sim$15 m s^{-1} (30 m s^{-1}) would evanesce [cf. *Marks and Eckermann*, 1995]. Thus any vertical shear in background winds will tend to reflect these waves more easily. Consistent with these inferences, Figure 2 reveals a low percentage of free-propagating 10 km horizontal wavelength GWs at 80 km altitude in all seasons. For horizontal wavelength longer than 10 km, slow ground-based phase speeds ($\leq$10 m s^{-1}) are less likely to reach the MLT than faster phase speeds. Figure 2 reveals that, in all seasons, the GWs with the highest probability of reaching the MLT are those with long horizontal wavelengths and fast ground-based phase speeds.

[40] Figure 3 plots probability distributions of the different criteria used by GROGRAT to terminate ray integrations in these experiments. These criteria are: (1) evanescence ($m^2 \leq 0$ at the source); (2) vertical reflection ($m^2 \leq 0$ away from source); (3) reached upper boundary (z = 100 km); (4) wave amplitude completely dissipated; (5) wave stalled near critical level (vertical group velocity criterion; see section 3); (6) wave propagated outside longitude-latitude range. Only options 3 and 6 are purely practical rather than physical criteria. (Option 4 is a proxy for critical-level removal.)

[41] In Figure 3a, only a few rays are evanescent at the source (except for λ_h = 10 km, c = 50 m s^{-1}), but many of the short wavelength rays soon become external through refraction and are reflected vertically. On the other hand, the slow waves (low phase speeds) are mostly dissipated or stalled near critical levels and are therefore not apt to carry significant momentum flux to high altitudes either. For the fast waves (c = 30 m s^{-1} and c = 50 m s^{-1}) with λ_h = 50 km the number of waves reaching the upper boundary at 100 km is significantly lower than those reaching 80 km (see Figure 2). This difference highlights significant deposition of GW momentum into the MLT between 80 and 100 km altitude.

[42] Equation (2) predicts that the horizontal wavelength $\lambda_{h,crit}$ delimiting the evanescent from the internal GW wavelength regime is inversely proportional to N. This yields more evanescent rays at the lower launch altitudes where N is smaller as shown in Figure 3b. Comparing Figures 3a and 3b we find a general increase of dissipated and stalled waves for slow phase-speed ($c \leq$ 10 m s^{-1}) GWs. The number of dissipated waves increases, because the waves are launched below a frequently present wind

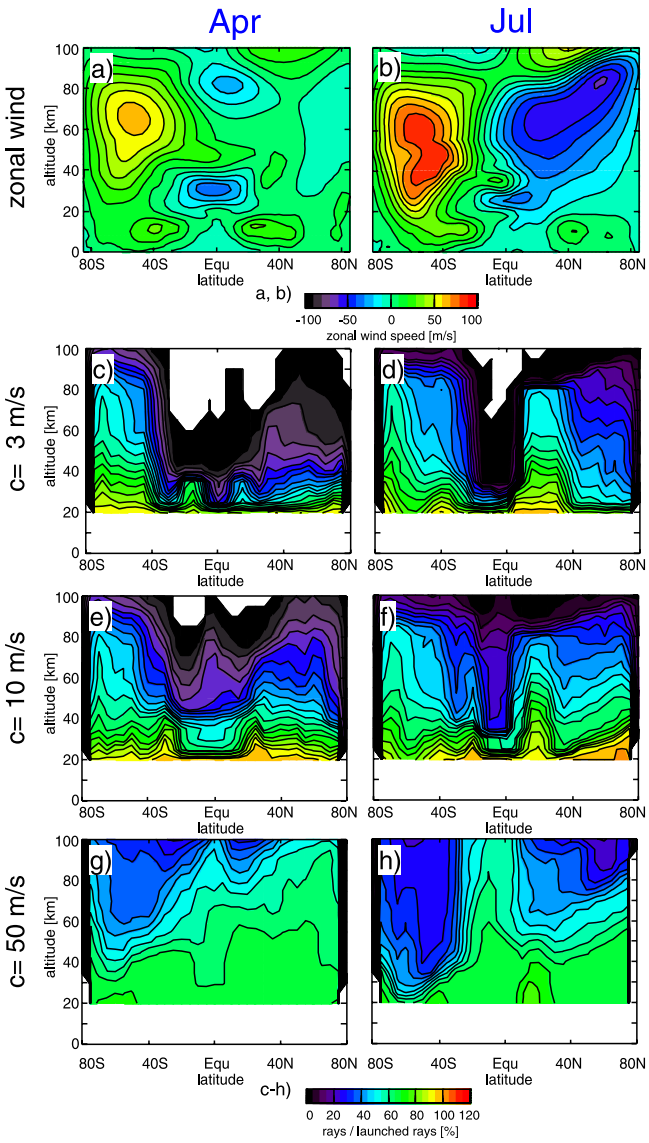

Figure 4. Altitude-latitude cross sections of the percentage of rays in an altitude-latitude bin. Shown are values for (left) April and (right) July. (a, b) Winds from Figure 1, and GROGRAT results for phase speeds of (c, d) 3, (e, f) 10, and (g, h) 50 m s^{-1}, respectively. Launch level is 20 km, and values are integrated over all four horizontal wavelengths.

reversal between the troposphere and stratosphere that also induces geographical variations discussed in section 4.2. Similar effects are seen in global model parameterizations [*Siskind et al.*, 2003].

[43] Having identified the processes largely responsible for filtering different parts of the wave spectrum by the background atmosphere, we can better interpret the seasonal dependences observed in Figure 2. The main difference between the different months is the different wind velocity in the middle atmosphere. Figure 1 shows, from the ground to 100 km, the zonal mean of the zonal winds which we have used for our ray-tracing experiment. At equinoxes the wind speeds are generally lower and therefore reflection of high phase speed, short horizontal wavelength waves at turning levels is less likely. For high phase-speed GWs the atmosphere is therefore more transparent at equinoxes than at the solstices.

[44] On the other hand, slow phase-speed waves ($c \leq 10$ m s^{-1}) can be refracted to longer vertical wavelengths and higher vertical group velocities if they propagate against the strong solstitial midlatitude stratospheric jets [cf. *Alexander*, 1998; *Preusse et al.*, 2006; *Eckermann et al.*, 2007]. Figure 2 shows that they are more likely to reach 80 km altitude at solstices than at equinoxes. However, only for July, 20 km launch altitude and horizontal wavelengths of 50 km the likelihood is close to 50%. In most other cases the likelihood for the slow waves to reach 80 km altitude is smaller than 30% and frequently even below 10%.

[45] Comparing rays launched in the troposphere (at 5 km altitude) with those launched above the tropopause (at 20 km), the probability for the rays launched at the lower level to reach 80 km altitude is nearly a factor of 2 lower than the probability for the rays launched at 20 km. One important controlling factor, as discussed earlier, is the lower buoyancy frequency in the troposphere, which affects predominantly the short horizontal wavelength waves and therefore shifts the boundary between external, nonpropagating waves and internal, propagating waves toward longer horizontal wavelengths. In addition, the wind reversal between tropospheric westerlies and stratospheric easterlies in summer adds strongly to the critical-level filtering of slow phase-speed waves.

4.2. Latitude-Height Distribution

[46] Different phase speeds exhibit strongly differing transparency distributions with height and latitude in Figure 4. Zonal mean results for three different phase speeds integrated over all horizontal wavelengths are shown for April and July. For low phase speeds, high wind speeds are favorable for GW propagation since waves propagating against the background winds are refracted to longer vertical wavelengths and therefore have higher probability of reaching the MLT. Consequently, a high percentage of the $c = 3$ m s^{-1} rays can reach high altitudes in the winter polar vortex of the southern hemisphere (80°S–40°S, July) and in the subtropical jet (10°N–40°N, July). The former result is consistent with observations showing strong penetration of quasi-stationary mountain waves from the southern Andes into the middle atmosphere during July [*Jiang et al.*, 2002], for example. Both features are less pronounced in April (equinox). In the tropics wind filtering due to the QBO can be discerned in the results. This is particularly pronounced in April. The first strong wind gradient occurs between 20 and 30 km and removes about half of the waves, the wind reversal between 30 and 40 km filters nearly all the remaining waves. This mechanism is well known, applying in a similar way to Kelvin waves and other tropical wave modes. Current estimates [*Dunkerton*, 1997] attribute the forcing of the QBO at about equal parts to large-scale tropical waves and smaller-scale GWs.

[47] For high phase speeds wave dissipation is less important, but waves can be either evanescent at the source or reflected vertically at a turning level. For both months the number of high phase-speed waves ($c = 50$ m s^{-1}) strongly decreases in the wind gradients below the stratospheric

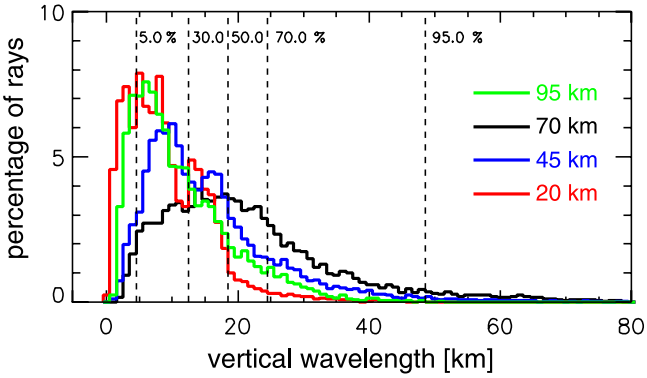

Figure 5. Histogram of the globally integrated distribution of the vertical wavelength at various altitudes for rays launched at 20 km in July. Also shown are percentiles for 70 km altitude. For details, see text.

wind maxima, where these waves are reflected, and the number of rays penetrating to the MLT peaks at the tropical latitudes where wind speeds are low in comparison to the mid and high latitudes.

4.3. Vertical Wavelengths

[48] The histograms in Figure 5 plot probability density functions (PDFs) of ray vertical wavelengths at various altitudes for the 20 km altitude launch spectrum. The distribution is a global integral for July. Only waves which reach at least 80 km altitude are shown. The PDFs are expressed as percentages, such that the integral over each histogram is always 100%. Owing to refraction by the background winds the histogram peaks shift back and forth in vertical wavelength with altitude. The relative importance of long vertical wavelength waves is largest at 70 km altitude near where the solsticial midlatitude jets peak in both hemispheres in Figure 4b. At 45 km altitude there is a hemispheric asymmetry between a strong winter polar vortex and, at this altitude, much weaker winds in the summer hemisphere. This could be responsible for the double-peak structure of the 45 km histogram in Figure 5. For the 70 km histogram we have also highlighted in Figure 5 the 5th, 30th, 50th, 70th and 95th percentiles; that is, the sum of the bins left of the 5% line is 5% of the total number of rays at this altitude. At 70 km altitude almost all waves have vertical wavelengths between 4 km (5th percentile) and 48 km (95th percentile).

[49] On the basis of the percentile values, Figure 6 systematically surveys the altitude and seasonal dependence of the vertical wavelength distribution. The results for 20 km launch altitude are considered, which provide a conservative estimate for those waves coupling the tropopause with the MLT. To better distinguish the curves, 5th, 50th and 95th percentiles are given as solid lines, 30 and 70th percentiles are given as dashed lines. For most curves the vertical wavelength steadily increases with altitude, reaches a maximum at around 70 km, decreases above 70 km and increases again above 90 km. Values are larger at the solstices than at the equinoxes owing to stronger solsticial stratospheric jets that refract waves to longer vertical wavelengths. This effect would be stronger if only regions of strong winds (e.g., midlatitudes) would be considered. The seasonal differences are most noticeable for the large percentile values, i.e., for the long vertical wavelengths. From Figure 6 one might conclude that an instrument measuring all waves between 3 km and 35 km vertical wavelength captures 90% of the waves propagating into the MLT. It should be noted, however, that there is a certain arbitrariness in the choice of wave properties at the source. While low vertical wavelengths are removed by filtering processes and the deduced limit is therefore well represented by the chosen launch distribution, the inclusion of larger phase-speed waves would shift the curves toward slightly longer wavelengths.

4.4. Horizontal Wavelength Limits

[50] The primary aim of this ray modeling is to quantify the horizontal wavelength limits imposed on short horizontal wavelength GWs by evanescence and vertical reflection and to compare this limits to the sensitivity ranges of different instrument types. From Figure 2 we have seen that waves of 10 km horizontal wavelengths very rarely reach the MLT and that fast waves of 50 km horizontal wavelength have a high probability of reaching 80 km altitude. Figure 2 shows the dependence on the ground based phase speed. However, satellite instruments measure the vertical wavelength of the waves which is determined by the intrinsic phase speed. In the following paragraphs we therefore deduce a short wavelength boundary that depends on the vertical wavelength of the waves.

[51] Since we focus on the limits imposed by wave reflection, we have chosen to launch GWs for which λ_h is of similar size to λ_z. For larger horizontal wavelengths, $k_h = (k^2 + l^2)^{1/2}$ becomes much smaller than $|m|$ and can be neglected in the denominator of the dispersion relation (equation (2)). In this midfrequency approximation (i.e., $f^2 \ll \hat{\omega}^2 \ll N^2$), the vertical wavelength becomes directly proportional to the intrinsic phase speed $\hat{c}$ and independent of the horizontal wavelength. For a 50 km horizontal wavelength GWs approximately satisfy the midfrequency approximation for all launched phase speeds and the waves

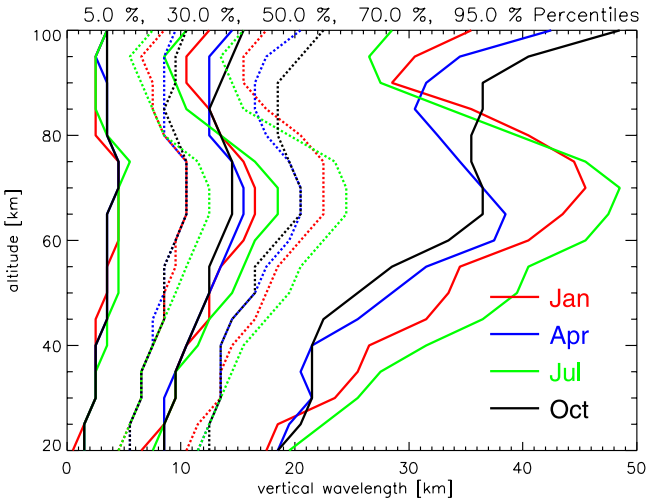

Figure 6. Altitude profiles of the 5th, 30th, 50th, 70th, and 95th percentiles (see Figure 5) of the globally integrated vertical wavelength distributions for the four different months.

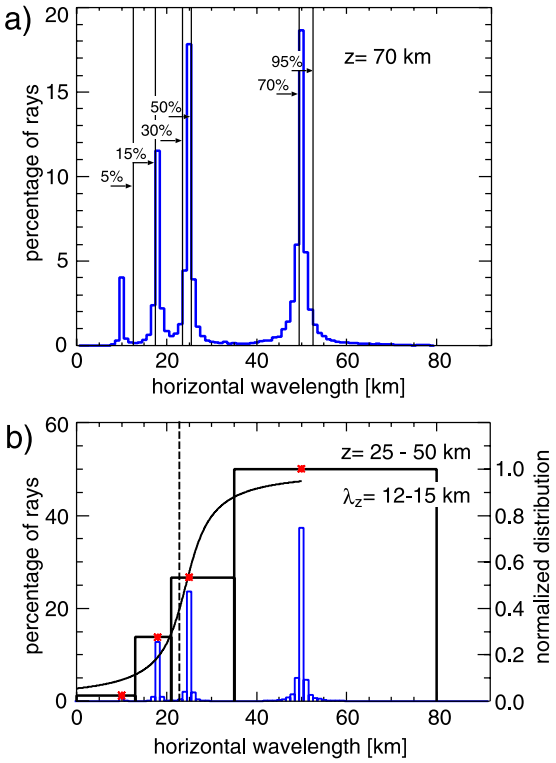

Figure 7. Histogram of the globally integrated horizontal wavelength distribution (a) at 70 km and (b) for altitudes between 25 and 50 km and vertical wavelengths between 12 and 15 km (blue curves). The wavelengths stay close to their initial values and the percentiles are close to the wavelength peaks. Figure 7b shows results of the rebinning to only four bins, the fit of a smooth function through the initial wavelengths (red crosses), and the deduction of a border wavelength (vertical dashed line) based on this fit.

with λ_h = 50 km are therefore representative of longer horizontal wavelengths. We have tested the dependence on the choice of horizontal wavelengths in Appendix B.

[52] Percentiles are a simple and robust method for characterizing the onset, center and width of smooth distributions. Since vertical wavelengths are continuously refracted by vertically varying background winds, the resulting histograms (see Figure 5) are quasi-continuous and percentiles can be applied. The method does not work, however, for the horizontal wavelengths: Horizontal wavelengths are refracted by horizontal wind shear. However, for the short horizontal GWs considered in this study the wavelength at higher altitudes remains close to its initial value. This is shown in Figure 7a, which gives the distribution of horizontal wavelengths at 70 km altitude (blue curve). The percentile values stay close to the main peaks, similar to initial findings at 65 km using the COSPAR International Reference Atmosphere (CIRA) reported by *Eckermann and Marks* [1997]. The noncontinuous nature of these distributions requires a different analysis method.

[53] The method we use to infer a short wavelength boundary from the horizontal wavelength distributions consisting of several sharp peaks is demonstrated in Figure 7b. The blue curve shows a horizontal wavelength histogram as in Figure 7a, but for selected vertical wavelengths between 12 and 15 km and integrated over altitudes between 25 and 50 km. The histogram shown in blue is rebinned to four coarse wavelength intervals around the initial horizontal wavelengths and the maximum value is normalized to 1.0 (black rectangles). Then the function

$$y = \frac{1}{\pi}\arctan(\zeta x + \eta) + \frac{1}{2} \tag{11}$$

is fitted to the data using the free parameters ζ and η. The function fits a smooth transition between limiting values of 0 and 1. The dashed vertical line shows where this function (black curve) equals 0.4, which is used to demark propagating waves from evanescent or reflected waves, hereafter referred to as the boundary wavelength $\lambda_{h,b}$. (We have also fitted a parabolic function with little change to the resulting $\lambda_{h,b}$ estimates).

[54] Figure 8 shows how $\lambda_{h,b}$ varies with vertical wavelength in the 25 to 50 km altitude interval. Results are shown for 5 km (dashed dotted lines) and 20 km (solid lines) launch altitude for the four months (indicated by color). At shorter vertical wavelengths $\lambda_{h,b}$ is also short. This agrees with equation (2) since shorter vertical wavelengths correspond to lower phase speeds. At the equinoxes the atmosphere allows shorter horizontal wavelength GWs to propagate upward relative to the solstices. The curves shift to longest $\lambda_{h,b}$ values in July, consistent with a higher probability of wave reflection in the strong solstitial stratospheric wind regimes. It should be noted that the most prominent MLT structures generally explained by GW momentum deposition, such as the cold summer mesopause and the zonal wind reversal in the summer MLT, are located above these strong wind regimes, which act to reflect the fast phase-speed short horizontal wavelength waves. The largest difference is between a launch level in the troposphere (5 km) and a launch level above the tropopause

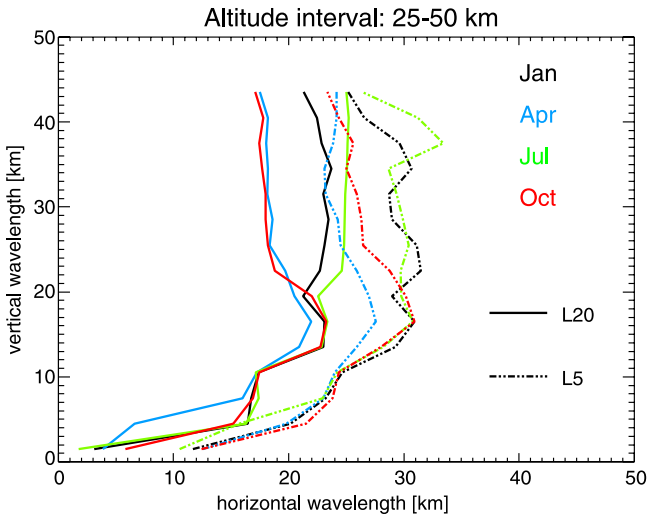

Figure 8. Boundary wavelength $\lambda_{h,b}$ between waves vertically propagating from the launch altitude to the MLT and evanescent or reflected waves. For details, see text.

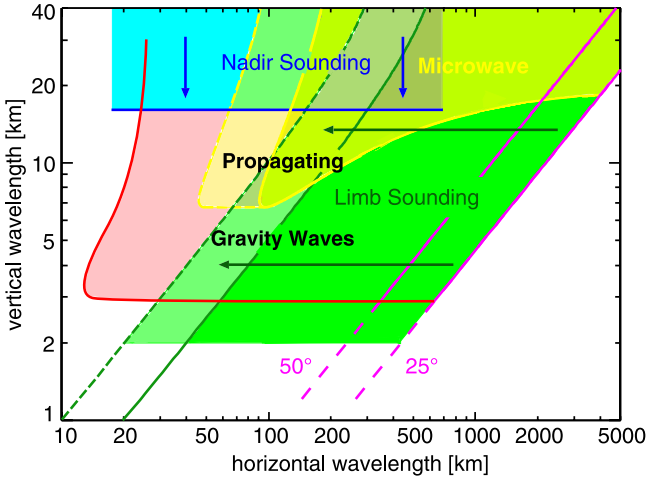

Figure 9. Range of gravity waves propagating from low to high altitudes delimited by the red and purple curves, compared to the sensitivity ranges of infrared and microwave limb sounding and nadir-viewing satellite instruments. The pink shaded area not covered by any of these instrument likely can be partially covered by a future instrument performing sublimb sounding of saturated radiance. For details, see text.

(20 km), which is also consistent with our earlier discussion of Figure 2.

5. Discussion

[55] Figure 9 compares the sensitivity ranges of different types of satellite remote-sensing instruments to the physical limits imposed on GW horizontal and vertical wavelengths as determined in section 4. From Figure 8 we obtain a short horizontal wavelength limit $\lambda_{h,b}$ of ~20–25 km for vertical wavelengths greater than ~15 km and $\lambda_{h,b} \simeq 10-15$ km at 3 km vertical wavelength. For a short vertical wavelength limit we use the 5th percentile from Figure 6, which is about 3 km. Together these values form the red line.

[56] The intrinsic frequency of GWs is limited by the Coriolis parameter such that

$$\hat{\omega}^2 > f^2 \Leftrightarrow \left|\frac{\hat{\omega}}{f}\right| > 1. \qquad (12)$$

[57] This does not yield a horizontal wavelength limit, if the ratio $|\hat{\omega}/f|$ can approach unity. CRISTA measurements indicate, however, that the ratio $|\hat{\omega}/f|$ remains larger than 1.4 in general [*Preusse et al.*, 2006], at least for vertical wavelengths $\lambda_z > 5$ km which CRISTA can resolve. The purple lines in Figure 9 show the corresponding wavelength limits implied by a limiting value of $|\hat{\omega}/f| = 1.4$ at 25° and 50° latitude.

[58] The red and purple lines in Figure 9 therefore delimit the range of upward propagating GWs which have the potential to transport GW momentum from the troposphere or tropopause upward into the MLT. This region is compared to the sensitivity ranges of the three remote-sensing techniques most frequently used to observe GWs in the middle atmosphere.

[59] The green shading in Figure 9 gives the range of wavelengths resolved by limb sounding of optically thin emissions (or occultations) based on the analytic radiative transfer solution derived by *Preusse et al.* [2002],

$$S(H,k,m) = \frac{1}{B}\frac{\partial B}{\partial T}\frac{\sqrt{\gamma}}{\sqrt[4]{\gamma^2+a^2}}\exp\left(-\frac{\gamma k_s^2}{4(\gamma^2+a^2)}\right), \qquad (13)$$

where $a = m/2R_{Earth} = 2\pi/(2\lambda_z R_{Earth})$, $k_s = 2\pi/\lambda_s$ is the wave number along the line of sight, $\gamma = 1/(2HR_{Earth})$, R_{Earth} the Earth's radius, H the pressure scale height, and $\frac{1}{B}\frac{\partial B}{\partial T}$ is the linear expansion in temperature T of the blackbody source function B. Temperature retrievals are simulated by normalizing to an infinite horizontal wavelength ($S(H, k, m)/S(H, 0, m)$). This analytic solution is in good agreement with explicit end-to-end numerical simulations for the CRISTA temperature retrievals [*Preusse et al.*, 2002] as well as with sensitivity estimates for temperature measurements by GPS radio occultations [*Lange and Jacobi*, 2003]. The solid green line in Figure 9 gives the horizontal wavelength, where the sensitivity for retrieved temperatures (i.e., $S(H, k, m)/S(H, 0, m)$) drops to 0.3. The sensitivity is estimated on the basis of the assumption that the GW phase fronts propagate perpendicular to the instrument's line of sight. This is the most unfavorable geometry for resolving the wave and so it seems realistic that in many cases waves with half of that horizontal wavelength could be observed [cf. *Preusse et al.*, 2002]. This is indicated in Figure 9 by the lighter-green shading between the solid and the dashed green line.

[60] The maximum achievable vertical resolution for limb sounders depends on the field of view, the vertical sampling rate, and the signal-to-noise level of the instrument. CRISTA attained about 3 km vertical resolution in its final temperature retrievals [*Riese et al.*, 1999; *Preusse et al.*, 2002], whereas SABER and HIRDLS have somewhat better vertical resolutions. Of all limb sounding instruments, GPS data have the best vertical resolution of ~1 km in standard retrievals [*Borsche et al.*, 2007] and even significantly higher resolution achieved in specialized retrievals [*Hocke et al.*, 2003].

[61] A second class of instruments traditionally used for GW analyses employ microwave limb sounding of saturated radiance [*Wu and Waters*, 1996]. We here use the 2D sensitivity function for these observations derived by *McLandress et al.* [2000], but for half the width of the UARS-MLS field of view, and show the range where this sensitivity function is larger than 0.3. This reduced field of view is reached by modern microwave sounders such as Aura MLS [*Wu and Eckermann*, 2008]. The GW wavelength regime covered by microwave instruments is shown in yellow in Figure 9. Again we can assume that at favorable viewing directions relative to the GW propagation direction, a factor 2 shorter horizontal wavelengths can be observed (light yellow).

[62] Most recently, cross-track scanning nadir-viewing instruments have also been employed for GW studies as a result of improvements in their spatial resolution and radiometric precision [*Eckermann and Wu*, 2006]. Their horizontal resolution is limited by the size of a measurement footprint, whereas their vertical resolution is limited by the width of the weighting functions of the thermal emissions they measure [*Eckermann and Wu*, 2006; *Alexander and*

Barnet, 2007]. In general, these instruments are sensitive only to waves with vertical wavelengths of ~15 km and longer. Nadir viewers are indicated by blue shading in Figure 9. It should be noted that for all these techniques the wavelength boundaries shift toward shorter wavelengths when observing very large amplitude events, since these remain visible even if the instrument's sensitivity is well below the assumed threshold of 0.3.

[63] Figure 9 reveals that together these three instrument types cover a reasonably broad range of the wavelengths typical of the vertically propagating GWs. However, there remains an important observational gap for GWs with horizontal wavelengths <60 km and vertical wavelengths <15 km indicated by pink shading in Figure 9. Numerical modeling indicates that convective forcing via the mechanical oscillator [*Fovell et al.*, 1992; *Piani et al.*, 2000] preferentially generates GWs in this range. This gap can likely be filled by sublimb remote sensing. For instance, *Dewan et al.* [1998] show two cases of concentric wave structures with horizontal wavelengths of 25 and 50 km and (presumably) vertical wavelengths of 16 and 18 km, respectively, emitted from mesoscale storm systems as observed by the sublimb MSX instrument. The sensitivity of sublimb sounders can be estimated by adapting the approach of *McLandress et al.* [2000] for estimating the MLS sensitivity but applied to sublimb angles between 5° and 30° and a 200 m width of the field of view (1σ width assuming a Gaussian shape). The results show that the complete range of horizontal wavelengths between 10 km and the sensitivity limit of limb sounding can be resolved.

[64] A multi-instrument monitoring strategy from space for all the free-propagating GW wavelength scales in the middle atmosphere therefore seems to be within reach. Future instruments should focus on improved sampling density across as well as along the orbital track. High-resolution along-track CRISTA sampling permitted absolute values of GW momentum flux to be inferred from temperature fluctuations [*Ern et al.*, 2004, 2006] and HIRDLS data will provide improved estimates due to this instrument's shorter along-track horizontal sampling distance [*Alexander et al.*, 2008]. Furthermore, vector estimates of GW momentum flux (i.e., estimates of the momentum flux value as well as wave propagation direction) would be possible using infrared limb imaging instruments [*Riese et al.*, 2005]. In addition, radiative transfer simulations show that the amplitudes of atmospheric GWs are underestimated, if the retrievals cannot take into account the horizontal fine structure of the GWs [*Preusse et al.*, 2002]. In current estimates of absolute values of momentum flux [*Ern et al.*, 2004, 2006; *Alexander et al.*, 2008] this is one of the leading error sources and uncertainties can be as large as a factor of 2 [*Ern et al.*, 2004]. Only if the instrument is viewing along track and samples the waves adequately can this underestimation be avoided [cf. *Ern et al.*, 2004, section 4.3].

[65] Having simultaneous information on the vertical as well as the horizontal wave structure permits GW characterization that then allows back-tracing studies to identify lower atmospheric wave sources [*Hertzog et al.*, 2001; *Wrasse et al.*, 2006]. For those waves in the wavelength regime where nadir and limb sounding sensitivities overlap, this allows for the combination of the horizontal wave image gained by the nadir viewer and the vertical wavelength and phase information obtained from the limb viewing instrument, which yields enhanced three-dimensional GW characterization and instrument cross validation.

6. Summary

[66] In this paper we have studied the transparency of the atmosphere to gravity waves of short horizontal wavelengths using theory and ray modeling. These waves, where present in the atmosphere, have a high potential for transporting and depositing eddy momentum into the mesosphere/lower thermosphere (MLT) region, since GW momentum flux is inversely proportional to the horizontal wavelength. The very shortest horizontal wavelength waves, however, are evanescent at the source or are vertically reflected by wind shear. Independent of the horizontal wavelength, higher phase-speed GWs attain longer vertical wavelengths and can potentially transport larger momentum fluxes, since the momentum flux of saturated waves is proportional to the vertical wavelength cubed.

[67] In this paper we have performed global ray-tracing experiments through a representative global atmosphere at four specific times (15 January, 15 April, 15 July and 15 October 2003) for a source of 6 different ground-based horizontal phase speeds and four different horizontal wavelengths located at two different launch altitudes of 5 km and 20 km. This allows us to investigate which GWs on average reach the MLT, which waves do not and the physical reasons why. While waves with high phase speeds and longer horizontal wavelengths ($\lambda_h \geq 50$ km) nearly always reach the MLT, waves with very short horizontal wavelengths are often reflected or are evanescent at their source and waves with low phase speeds are frequently dissipated near critical levels.

[68] Wave reflection occurs in regions with high wind velocities, in particular in the winter polar and the summer subtropical stratospheric jets at solstices. This is particularly interesting since the cold summer mesopause and the wind reversal in the MLT are located above such jets where the short horizontal wavelength waves are filtered. Wave dissipation, by contrast, is found in weak wind regimes and in particular in the vicinity of wind reversals.

[69] A horizontal wavelength boundary $\lambda_{h,b}$ of ~2–30 km demarks those waves with a high likelihood to propagate upward ($\lambda_h > \lambda_{h,b}$) and those likely to be evanescent at the source or vertically reflected ($\lambda_h < \lambda_{h,b}$). $\lambda_{h,b}$ varies with season and tends to have higher values at solstices and for low-altitude launch levels.

[70] No single satellite instrument can resolve the whole wavelength range of all the propagating GWs in the middle atmosphere, but a synergetic use of different kinds of satellite observing techniques, such as optically thin and saturated limb observations as well as saturated sublimb and cross-track nadir emissions can approach the goal of global monitoring the complete 3D wavelength range of all those GWs potentially carrying momentum from the troposphere/tropopause region into the MLT.

[71] Largest improvements in satellite GW research in the future are to be expected from improved analysis techniques and synergetic use of multi-instrument data from many satellites, or even preferentially, from a dedicated GW mission combining several such instruments on the same

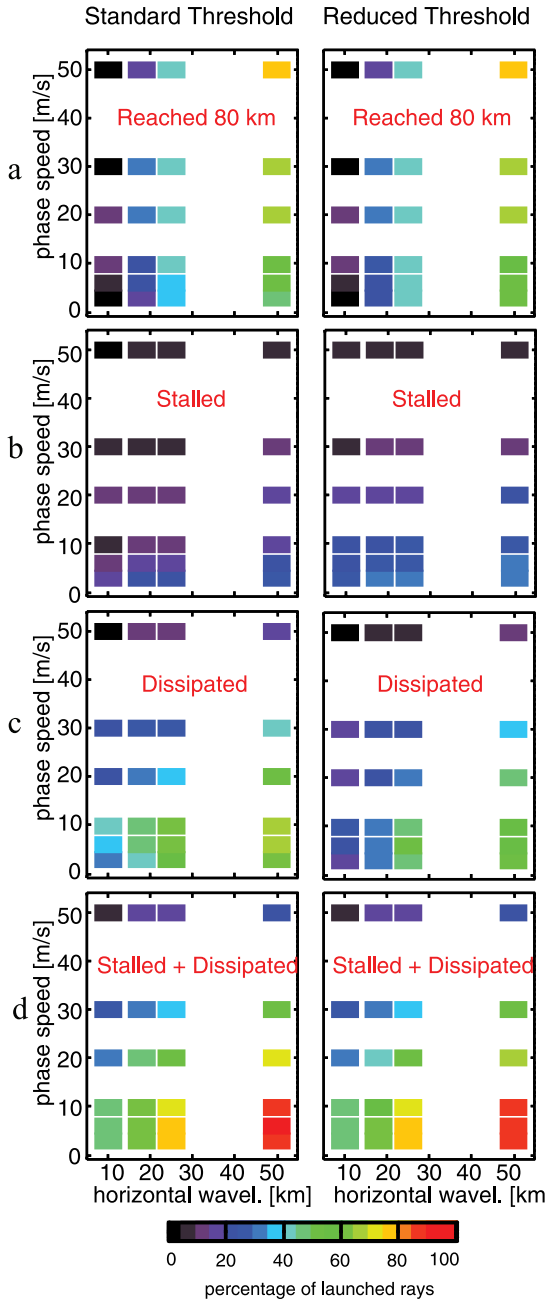

Figure A1. Comparison between (left) 1% relative amplitude threshold used in standard runs and (right) 1000 times reduced threshold. For details, see text.

platform for synchronized common-volume measurements. High priority in instrument development should be given to increased spatial sampling both along and across track. This can be gained, for instance, by proposed new infrared limb imagers providing a fully resolved three-dimensional image of the wave fronts from a single instrument.

Appendix A: Dependence on the Dissipation Threshold

[72] When a gravity wave approaches a critical level, i.e., when the background wind speed approaches the ground based phase speed, then the intrinsic frequency, the vertical group velocity, the vertical wavelength and the saturation amplitude all approach zero, too. Since the vertical group velocity becomes small, a ray tracer approaches the critical level in very fine steps causing large computational costs. However, very close to the critical level the effects of such a wave are very small because of the small saturation amplitude. Therefore in the standard runs of this paper waves are terminated when the actual amplitude of the wave falls below 1% of the launch amplitude. In this appendix we show that this affects waves close to critical levels and does not remove rays with small amplitudes in the lower atmosphere which could grow to large amplitudes in the MLT causing large accelerations there.

[73] GROGRAT uses two termination criteria which compete below a critical level: waves that fall below a minimum relative amplitude with respect to the launch amplitude are called "dissipated," waves with group velocities below a threshold are called "stalled" (see sections 3 and 4.1). In Figure A1 we compare an experiment with a minimum relative amplitude threshold of 1% (Figure A1, left) to an experiment with a 1000 times smaller threshold for July and 20 km launch level (Figure A1, right). Figure A1a shows the percentage of all rays reaching at least 80 km altitude (see Figure 2), Figures A1b and A1c show the percentage of stalled and dissipated waves, respectively (see Figure 3), and Figure A1d shows the sum of stalled and dissipated rays. There are some minor changes (one color step or less) in the number of waves reaching 80 km altitude or more. However, the relative importance of the two termination criteria shifts for the run with reduced minimum amplitude threshold. In particular for the short horizontal wavelength waves the number of dissipated waves is significantly reduced, but this is compensated by an equally increased number of stalled waves (changes in the sum of both termination criteria are again very minor). The experiment therefore confirms that the minimum amplitude criterion indeed removes waves below critical levels and does not filter other waves of low amplitudes, the latter potentially having large impact on the MLT.

Appendix B: Dependence on the Chosen Launch Distribution

[74] In this study we are primarily interested in the effects of wave reflection and wave evanescence on the ability of

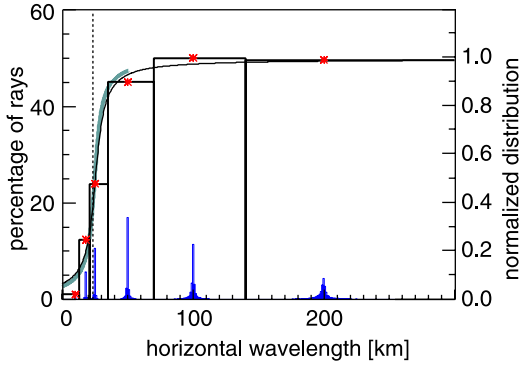

Figure B1. As in Figure 7b but including mesoscale GWs of 100 km and 200 km horizontal wavelength at launch level.

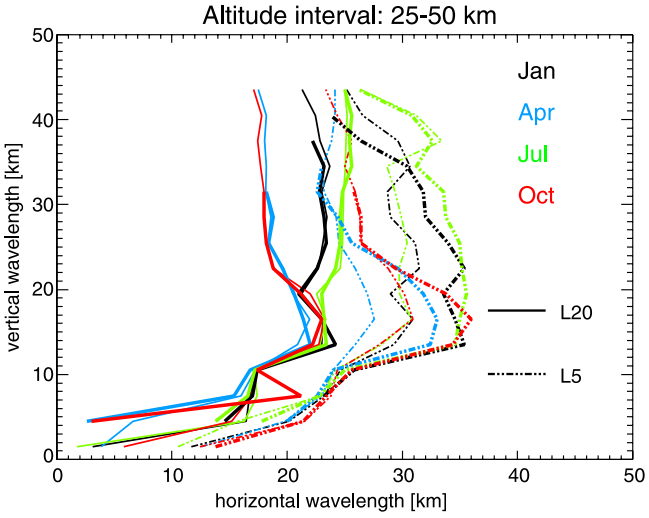

Figure B2. Comparison of the boundary wavelength $\lambda_{h,b}$ between (thin lines) the original experiment and (bold lines) the experiment extended by two mesoscale components of 100 km and 200 km horizontal wavelength.

waves to propagate upward from sources in the troposphere or at the tropopause toward the MLT. We therefore chose wave components for which horizontal and vertical wavelength are of comparable size. However, for the deduction of the boundary wavelength $\lambda_{h,b}$ delimiting the propagating from the evanescent or reflected waves we have assumed that at 50 km horizontal wavelength the waves would satisfy the mid frequency approximation and that these waves are representative of longer horizontal wavelength GWs. In the strong solsticial winds this assumption is not always valid. We therefore test, in this appendix, whether the choice of launched waves and, in particular, the omission of true midfrequency components with mesoscale horizontal wavelengths affects the determined boundary wavelength $\lambda_{h,b}$.

[75] In section 3 we describe the setup of the ray-tracing experiments. In particular, we have chosen six phase speeds and four horizontal wavelength components. We now extend these experiments by two further horizontal wavelengths of $\lambda_h = 100$ km and $\lambda_h = 200$ km. Figure B1 is for the same data as Figure 7b supplemented with the two additional horizontal wavelengths (see section 4.4 for a detailed description). Since the integral of the histogram (blue curve) is normalized to 100%, the percentage value for the four shortest wavelengths is now smaller than in Figure 7b. The maximum value of the coarse histogram (shown in black) is normalized to one (y axis on the right) and therefore Figure 7b and Figure B1 are comparable. The arcus tangens curve given in grey is the original fit from only four horizontal wavelength components (as in Figure 7), the black curve shows the fit through all six components. It can be seen that the differences are small.

[76] In Figure B2 we compare the deduced boundary wavelengths $\lambda_{h,b}$. The thin lines reproduce the results of the fits from four horizontal wavelengths shown in Figure 8. Overplotted (bold lines) are the results from six wavelength components. For most vertical wavelength ranges the results are almost indiscernible, in particular for the 20 km launch level. For the 5 km launch level and vertical wavelengths around 15 km the horizontal wavelengths are somewhat larger. The intraseasonal variation and the general shape remains unchanged. However, the fits for six horizontal wavelength components do not work for either very short or very long vertical wavelengths. At slow phase speeds most waves are dissipated or stall below critical levels. Short horizontal wavelengths have higher group velocities and their vertical wavelengths are somewhat longer (see equation (5)) and therefore the midfrequency waves are even more susceptible to dissipation than the short horizontal wavelength waves. Therefore the number of waves decreases at longer horizontal wavelengths and the arcus tangens fit fails. Likewise, only very strong background winds can refract the two longer horizontal wavelength components to very long vertical wavelengths (larger than ~30 km) whereas shorter horizontal wavelength waves again attain longer vertical wavelengths according to (5). Therefore the boundary wavelength curves determined also from the mesoscale components cover a reduced vertical wavelength range but otherwise confirm the results we have obtained.

[77] **Acknowledgments.** We thank Jens Oberheide and Raymond Roble for providing the TIME-GCM model output. S.D. Eckermann's work was supported by NASA's Geospace Sciences SR & T Program. We thank two anonymous reviewers for their careful reading of the manuscript and one reviewer for valuable comments and in particular for comments on the short horizontal wavelength GWs.

References

Akmaev, R. A. (2001), Simulation of large-scale dynamics in the mesosphere and lower thermosphere with the Doppler-spread parameterization of gravity waves: 1. Implementation and zonal mean climatologies, *J. Geophys. Res.*, *106*, 1193–1204.

Alexander, M. J. (1998), Interpretations of observed climatological patterns in stratospheric gravity wave variance, *J. Geophys. Res.*, *103*, 8627–8640.

Alexander, M. J., and C. Barnet (2007), Using satellite observations to constrain parameterizations of gravity wave effects for global models, *J. Atmos. Sci.*, *64*, 1652–1665.

Alexander, M. J., and T. J. Dunkerton (1999), A spectral parameterization of mean-flow forcing due to breaking gravity waves, *J. Atmos. Sci.*, *56*, 4167–4182.

Alexander, M. J., T. Tsuda, and R. A. Vincent (2002), On the latitudinal variations observed in gravity waves with short vertical wavelengths, *J. Atmos. Sci.*, *59*, 1394–1404.

Alexander, M. J., et al. (2008), Global estimates of gravity wave momentum flux from High Resolution Dynamics Limb Sounder observations, *J. Geophys. Res.*, *113*, D15S18, doi:10.1029/2007JD008807.

Bacmeister, J. T., S. D. Eckermann, P. A. Newman, L. Lait, K. R. Chan, M. Loewenstein, M. H. Porffitt, and B. L. Gary (1996), Stratospheric horizontal wavenumber spectra of winds, potential temperature, and atmospheric tracers observed by high-altitude aircraft, *J. Geophys. Res.*, *101*, 9441–9470.

Borsche, M., G. Kirchengast, and U. Foelsche (2007), Tropical tropopause climatology as observed with radio occultation measurements from CHAMP compared to ECMWF and NCEP analyses, *Geophys. Res. Lett.*, *34*, L03702, doi:10.1029/2006GL027918.

Charron, M., E. Manzini, and C. D. Warner (2002), Intercomparison of gravity wave parameterizations: Hines Doppler-spread and Warner and McIntyre ultra-simple schemes, *J. Meteorol. Soc. Jpn.*, *80*, 335–345.

de la Torre, A., T. Schmidt, and J. Wickert (2006), A global analysis of wave potential energy in the lower stratosphere derived from 5 years of GPS radio occultation data with CHAMP, *Geophys. Res. Lett.*, *33*, L24809, doi:10.1029/2006GL027696.

Dewan, E. M., R. H. Picard, R. R. O'Neil, H. A. Gardiner, J. Gibson, J. D. Mill, E. Richards, M. Kendra, and W. O. Gallery (1998), MSX satellite observations of thunderstorm-generated gravity waves in mid-wave infrared images of the upper stratosphere, *Geophys. Res. Lett.*, *25*, 939–942.

Dörnbrack, A., T. Birner, A. Fix, H. Flentje, A. Meister, H. Schmid, E. V. Browell, and M. J. Mahoney (2002), Evidence for inertia gravity waves forming polar stratospheric clouds over Scandinavia, *J. Geophys. Res.*, *107*(D20), 8287, doi:10.1029/2001JD000452.

Dunkerton, T. J. (1997), The role of gravity waves in the quasi-biennial oscillation, *J. Geophys. Res.*, *102*, 26,053–26,076.
Eckermann, S. D., and C. J. Marks (1997), GROGRAT: A new model of the global propagation and dissipation of atmospheric gravity waves, *Adv. Space Res.*, *20*, 1253–1256.
Eckermann, S. D., and P. Preusse (1999), Global measurements of stratospheric mountain waves from space, *Science*, *286*, 1534–1537.
Eckermann, S. D., and D. L. Wu (2006), Imaging gravity waves in lower stratospheric AMSU-A radiances, Part 1: Simple forward model, *Atmos. Chem. Phys.*, *6*, 3325–3341.
Eckermann, S. D., et al. (2006), Imaging gravity waves in lower stratospheric AMSU-A radiances, Part 2: Validation case study, *Atmos. Chem. Phys.*, *6*, 3343–3362.
Eckermann, S. D., J. Ma, D. L. Wu, and D. Broutman (2007), A three-dimensional mountain wave imaged in satellite radiance throughout the stratosphere: Evidence of the effects of directional wind shear, *Q. J. R. Meteorol. Soc.*, *133*, 1959–1975.
Ern, M., P. Preusse, M. J. Alexander, and C. D. Warner (2004), Absolute values of gravity wave momentum flux derived from satellite data, *J. Geophys. Res.*, *109*, D20103, doi:10.1029/2004JD004752.
Ern, M., P. Preusse, and C. D. Warner (2005), A comparison between CRISTA satellite data and Warner and McIntyre gravity wave parameterization scheme: Horizontal and vertical wavelength filtering of gravity wave momentum flux, *Adv. Space Res.*, *35*, 2017–2023, doi:10.1016/j.asr.2005.04.109.
Ern, M., P. Preusse, and C. D. Warner (2006), Some experimental constraints for spectral parameters used in the Warner and McIntyre parameterization scheme, *Atmos. Chem. Phys.*, *6*, 4361–4381.
Ern, M., P. Preusse, M. Krebsbach, M. G. Mlynczak, and J. M. Russell III (2007), Equatorial wave analysis from SABER and ECMWF temperatures, *Atmos. Chem. Phys. Discuss.*, *7*, 11,685–11,723.
Espy, P. J., G. O. L. Jones, G. R. Swenson, J. Tang, and M. J. Taylor (2004), Seasonal variations of the gravity wave momentum flux in the Antarctic mesosphere and lower thermosphere, *J. Geophys. Res.*, *109*, D23109, doi:10.1029/2003JD004446.
Espy, P. J., R. E. Hibbins, G. R. Swenson, J. Tang, M. J. Taylor, D. M. Riggin, and D. C. Fritts (2006), Regional variations of mesospheric gravity-wave momentum flux over Antarctica, *Ann. Geophys.*, *24*, 81–88.
Fetzer, E. J., and J. C. Gille (1994), Gravity wave variances in LIMS temperatures, I, Variability and comparison with background winds, *J. Atmos. Sci.*, *51*, 2461–2483.
Fovell, R., D. Durran, and J. R. Holton (1992), Numerical simulations of convectively generated stratospheric gravity waves, *J. Atmos. Sci.*, *49*, 1427–1442.
Fritts, D. C., and M. J. Alexander (2003), Gravity wave dynamics and effects in the middle atmosphere, *Rev. Geophys.*, *41*(1), 1003, doi:10.1029/2001RG000106.
Fritts, D. C., S. L. Vadas, and Y. Yamada (2002), An estimate of strong local body forcing and gravity wave radiation based on OH airglow and meteor radar observations, *Geophys. Res. Lett.*, *29*(10), 1429, doi:10.1029/2001GL013753.
Hagan, M. E., J. M. Forbes, and F. Vial (1995), On modeling migrating solar tides, *Geophys. Res. Lett.*, *22*, 893–896.
Hamilton, K., R. J. Wilson, and R. S. Hemler (1999), Middle atmosphere simulated with high vertical and horizontal resolution versions of a GCM: Improvements in the cold pole bias and generation of a QBO-like oscillation in the tropics, *J. Atmos. Sci.*, *56*, 3829–3846.
Hertzog, A., C. Souprayen, and A. Hauchecorne (2001), Observation and backward trajectory of an inertio-gravity wave in the lower stratosphere, *Ann. Geophys.*, *19*, 1141–1155.
Hines, C. O. (1997), Doppler-spread parameterization of gravity-wave momentum deposition in the middle atmosphere. Part 1: Basic formulation, *J. Atmos. Solar Terr. Phys.*, *59*, 371–386.
Hocke, K., K. Igarashi, and T. Tsuda (2003), High-resolution profiling of layered structures in the lower stratosphere by GPS occultation, *Geophys. Res. Lett.*, *30*(8), 1426, doi:10.1029/2002GL016566.
Holton, J. R. (1982), The role of gravity wave induced drag and diffusion in the momentum budget of the mesosphere, *J. Atmos. Sci.*, *39*, 791–799.
Horinouchi, T., et al. (2003), Tropical cumulus convection and upward-propagating waves in middle-atmospheric GCMs, *J. Atmos. Sci.*, *60*, 2765–2782.
Iwasaki, T., S. Yamada, and K. Tada (1989), A parameterization scheme of orographic gravity wave drag with two different vertical partitionings, Part I: Impacts on medium-range forecasts, *J. Meteorol. Soc. Jpn.*, *67*, 11–27.
Jiang, J. H., D. L. Wu, and S. D. Eckermann (2002), Upper Atmosphere Research Satellite (UARS) MLS observations of mountain waves over the Andes, *J. Geophys. Res.*, *107*(D20), 8273, doi:10.1029/2002JD002091.
Jiang, J. H., B. Wang, K. Goya, K. Hocke, S. D. Eckermann, J. Ma, D. L. Wu, and W. J. Read (2004), Geographical distribution and interseasonal variability of tropical deep convection: UARS MLS observations and analyses, *J. Geophys. Res.*, *109*, D03111, doi:10.1029/2003JD003756.
Kim, Y.-J., S. D. Eckermann, and H.-Y. Chun (2003), An overview of the past, present and future of gravity-wave drag parameterization for numerical climate and weather prediction models, *Atmos. Ocean*, *41*, 65–98.
Lane, T. P., and J. C. Knievel (2005), Some effects of model resolution on simulated gravity waves generated by deep, mesoscale convection, *J. Atmos. Sci.*, *62*, 3408–3419.
Lane, T. P., M. J. Reeder, and T. L. Clark (2001), Numerical modeling of gravity wave generation by deep tropical convection, *J. Atmos. Sci.*, *58*, 1249–1274.
Lange, M., and C. Jacobi (2003), Analysis of gravity waves from radio occultation measurements, in *First CHAMP Mission Results for Gravity, Magnetic and Atmospheric Studies*, edited by C. Reigber, H. Lühr, and P. Schwintzer, pp. 479–484, Springer, Berlin.
Manzini, E., and N. A. McFarlane (1998), The effect of varying the source spectrum of a gravity wave parameterization in a middle atmosphere general circulation model, *J. Geophys. Res.*, *103*, 31,523–31,539.
Manzini, E., N. A. McFarlane, and C. McLandress (1997), Impact of the Doppler spread parameterization on the simulation of the middle atmosphere circulation using the MA/ECHAM4 general circulation model, *J. Geophys. Res.*, *102*, 25,751–25,762.
Marks, C. J., and S. D. Eckermann (1995), A three-dimensional nonhydrostatic ray-tracing model for gravity waves: Formulation and preliminary results for the middle atmosphere, *J. Atmos. Sci.*, *52*, 1959–1984.
McLandress, C. (1998), On the importance of gravity waves in the middle atmosphere and their parameterization in general circulation models, *J. Atmos. Solar Terr. Phys.*, *60*, 1357–1383.
McLandress, C., M. J. Alexander, and D. L. Wu (2000), Microwave Limb Sounder observations of gravity waves in the stratosphere: A climatology and interpretation, *J. Geophys. Res.*, *105*, 11,947–11,967.
Nastrom, G. D., and D. C. Fritts (1992), Sources of mesoscale variability of gravity waves. Part I: Topographic excitation, *J. Atmos. Sci.*, *49*, 101–110.
Oberheide, J., Q. Wu, T. L. Killeen, M. E. Hagan, and R. G. Roble (2006), Diurnal nonmigrating tides from TIDI wind data: Monthly climatologies and seasonal variations, *J. Geophys. Res.*, *111*, A10S03, doi:10.1029/2005JA011491.
Pfister, L., S. Scott, M. Loewenstein, S. Bowen, and M. Legg (1993), Mesoscale disturbances in the tropical stratosphere excited by convection: Observations and effects on the stratospheric momentum budget, *J. Atmos. Sci.*, *50*, 1058–1075.
Piani, C., D. Durran, M. J. Alexander, and J. R. Holton (2000), A numerical study of three-dimensional gravity waves triggered by deep convection and their role in the dynamics of the QBO, *J. Atmos. Sci.*, *57*, 3689–3702.
Preusse, P., and M. Ern (2005), Indication of convectively generated gravity waves observed by CLAES, *Adv. Space Res.*, *35*, 1987–1991, doi:10.1016/j.asr.2004.09.005.
Preusse, P., G. Eidmann, S. D. Eckermann, B. Schaeler, R. Spang, and D. Offermann (2001), Indications of convectively generated gravity waves in CRISTA temperatures, *Adv. Space Res.*, *27*, 1653–1658.
Preusse, P., A. Dörnbrack, S. D. Eckermann, M. Riese, B. Schaeler, J. Bacmeister, D. Broutman, and K. U. Grossmann (2002), Space based measurements of stratospheric mountain waves by CRISTA: 1. Sensitivity, analysis method, and a case study, *J. Geophys. Res.*, *107*(D23), 8178, doi:10.1029/2001JD000699.
Preusse, P., et al. (2006), Tropopause to mesopause gravity waves in August: Measurement and modeling, *J. Atmos. Solar Terr. Phys.*, *68*, 1730–1751.
Queney, P. (1948), The problem of airflow over mountains: A summary of theoretical studies, *Bull. Am. Meteorol. Soc.*, *29*, 16–27.
Riese, M., R. Spang, P. Preusse, M. Ern, M. Jarisch, D. Offermann, and K. U. Grossmann (1999), Cryogenic Infrared Spectrometers and Telescopes for the Atmosphere (CRISTA) data processing and atmospheric temperature and trace gas retrieval, *J. Geophys. Res.*, *104*, 16,349–16,367.
Riese, M., F. Friedl-Vallon, R. Spang, P. Preusse, C. Schiller, L. Hoffmann, P. Konopka, H. Oelhaf, T. von Clarmann, and M. Höpfner (2005), GLObal limb Radiance Imager for the Atmosphere (GLORIA): Scientific objectives and mission concept, *Adv. Space Res.*, *36*, 989–995.
Roble, R. G., and E. C. Ridley (1994), A thermosphere-ionosphere-mesosphere-electrodynamics general circulation model (time-GCM): Equinox solar cycle minimum simulations (30–500 km), *Geophys. Res. Lett.*, *21*, 417–420.
Salby, M. L., and R. R. Garcia (1987), Transient response to localized episodic heating in the tropics. Part I: Excitation and short-time near-field behavior, *J. Atmos. Sci.*, *44*, 458–498.
Schoeberl, M. R. (1985), The penetration of mountain waves into the middle atmosphere, *J. Atmos. Sci.*, *42*, 2856–2864.

Sentman, D. D., E. M. Wescott, R. H. Picard, J. R. Winick, H. C. Stenbaek-Nielsen, E. M. Dewan, D. R. Moudry, F. T. Sao Sabbas, M. J. Heavner, and J. Morrill (2003), Simultaneous observations of mesospheric gravity waves and sprites generated by a midwestern thunderstorm, *J. Atmos. Solar Terr. Phys.*, *65*, 537–550.

Siskind, D. E., S. D. Eckermann, J. P. McCormack, M. J. Alexander, and J. T. Bacmeister (2003), Hemispheric differences in the temperature of the summertime stratosphere and mesosphere, *J. Geophys. Res.*, *108*(D2), 4051, doi:10.1029/2002JD002095.

Smith, S. M., J. Scheer, E. R. Reisin, J. Baumgardner, and M. Mendillo (2006), Characterization of exceptionally strong mesospheric wave events using all-sky and zenith airglow observations, *J. Geophys. Res.*, *111*, A09309, doi:10.1029/2005JA011197.

Suzuki, S., K. Shiokawa, Y. Otsuka, T. Ogawa, K. Nakamura, and T. Nakamura (2007a), A concentric gravity wave structure in the mesospheric airglow images, *J. Geophys. Res.*, *112*, D02102, doi:10.1029/2005JD006558.

Suzuki, S., K. Shiokawa, Y. Otsuka, T. Ogawa, M. Kubota, M. Tsutsumi, T. Nakamura, and D. C. Fritts (2007b), Gravity wave momentum flux in the upper mesosphere derived from OH airglow imaging measurements, *Earth Planets Space*, *59*, 421–428.

Swenson, G. R., R. Haque, W. Yang, and C. S. Gardner (1999), Momentum and energy fluxes of monochromatic gravity waves observed by an OH imager at Starfire Optical Range, New Mexico, *J. Geophys. Res.*, *104*, 6067–6080.

Tang, J., A. Z. Liu, and G. R. Swenson (2002), High frequency gravity waves observed in OH airglow at Starfire Optical Range, NM: Seasonal variations in momentum flux, *Geophys. Res. Lett.*, *29*(20), 1966, doi:10.1029/2002GL015794.

Tang, J., G. R. Swenson, A. Z. Liu, and F. Kamalabadi (2005), Observational investigations of gravity wave momentum flux with spectroscopic imaging, *J. Geophys. Res.*, *110*, D09S09, doi:10.1029/2004JD004778.

Taylor, M. J., and M. A. Hapgood (1988), Identification of a thunderstorm as a source of short period gravity waves in the upper atmospheric nightglow emissions, *Planet. Space Sci.*, *36*, 975–985.

Taylor, M. J., M. A. Hapgood, and P. Rothwell (1987), Observations of gravity wave propagation in the OI (557.7 nm), Na (589.2 nm) and the near infrared OH nightglow emissions, *Planet. Space Sci.*, *35*, 413–427.

Tsuda, T., T. E. VanZandt, M. Mizumoto, S. Kato, and S. Fukao (1991), Spectral analysis of temperature and Brunt-Vaisala frequency fluctuations observed by radiosondes, *J. Geophys. Res.*, *96*, 17,265–17,278.

Tsuda, T., M. Nishida, C. Rocken, and R. H. Ware (2000), A global morphology of gravity wave activity in the stratosphere revealed by the GPS occultation data (GPS/MET), *J. Geophys. Res.*, *105*, 7257–7273.

Vincent, R. A., A. Hertzog, G. Boccara, and F. Vial (2007), Quasi-Lagrangian superpressure balloon measurements of gravity-wave momentum fluxes in the polar stratosphere of both hemispheres, *Geophys. Res. Lett.*, *34*, L19804, doi:10.1029/2007GL031072.

Wang, L., M. A. Geller, and M. J. Alexander (2005), Spatial and temporal variations of gravity wave parameters. Part I: Intrinsic frequency, wavelength, and vertical propagation direction, *J. Atmos. Sci.*, *62*, 125–142.

Warner, C. D., and M. E. McIntyre (2001), An ultra-simple spectral parameterization for non-orographic gravity waves, *J. Atmos. Sci.*, *58*, 1837–1857.

Wrasse, C. M., et al. (2006), Mesospheric gravity waves observed near equatorial and low-middle latitude stations: Wave characteristics and reverse ray tracing results, *Ann. Geophys.*, *24*, 3229–3240.

Wu, D. L., and S. D. Eckermann (2008), Global gravity variances from Aura MLS: Characteristics and interpretation, *J. Atmos. Sci.*, in press.

Wu, D. L., and J. W. Waters (1996), Gravity-wave-scale temperature fluctuations seen by the UARS MLS, *Geophys. Res. Lett.*, *23*, 3289–3292.

Wu, D. L., and F. Zhang (2004), A study of mesoscale gravity waves over the North Atlantic with satellite observations and a mesoscale model, *J. Geophys. Res.*, *109*, D22104, doi:10.1029/2004JD005090.

Wu, D. L., P. Preusse, S. D. Eckermann, J. H. Jiang, M. de la Torre Juarez, L. Coy, B. Lawrence, and D. Y. Wang (2006), Remote sounding of atmospheric gravity waves with satellite limb and nadir techniques, *Adv. Space Res.*, *37*, 2269–2277.

S. D. Eckermann, Space Science Division, Code 7646, Naval Research Laboratory, Washington, DC 20375-5352, USA. (stephen.eckermann@nrl.navy.mil)

M. Ern and P. Preusse, Institut für Chemie und Dynamik der Geosphäre, ICG-1: Stratosphäre, Forschungszentrum Jülich GmbH, D-52425 Jülich, Germany. (p.preusse@fz-juelich.de)